Solid State Ionics 441 (2026) 117205

Contents lists available at ScienceDirect

Solid State Ionics

journal homepage: www.elsevier.com/locate/ssi

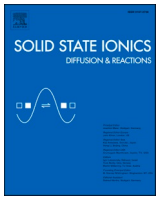

Tuning functional properties via Fe/Al ratio in the franklinite–gahnite ($ZnFe_2O_4$-$ZnAl_2O_4$) solid solution series

Meriem Machitouen [a,b], Patrick Mowe [a], Johannes Spiegel [c], Susanna Krämer [a], Rüdiger-A. Eichel [c,d,e], Martin Winter [a,f], Thomas Jüstel [b], Anna Windmüller [c], Kerstin Neuhaus [a,*]

[a] Forschungszentrum Jülich GmbH, Institute of Energy Materials and Devices (IMD-4): Helmholtz-Institute Münster (HI MS), Corrensstr. 46, 48149 Münster, Germany
[b] FH Münster University of Applied Sciences, Department of Chemical Engineering, Stegerwaldstraße 39, 48565 Steinfurt, Germany
[c] Forschungszentrum Jülich GmbH, Institute of Energy Technologies (IET-1): Fundamental Electrochemistry, 52425 Jülich, Germany
[d] Institute of Physical Chemistry, RWTH Aachen University, Aachen 52074, Germany
[e] Faculty of Mechanical Engineering, RWTH Aachen University, Aachen 52074, Germany
[f] University of Münster, MEET Battery Research Center, Institute of Physical Chemistry, Corrensstr. 46, 48149 Münster, Germany

ARTICLE INFO

Keywords:
Zinc ferrite
Zinc battery
Band gap
Conductivity
Magnetic susceptibility

ABSTRACT

In this study, a comprehensive investigation of the structure-property relationship in the solid solution series $ZnFe_{2-x}Al_xO_4$ with x = 0.0 to 2.0 is provided. Measurements of the electrical conductivity, optical band gap, magnetic susceptibility, and other relevant parameters are discussed in dependence on the aluminum concentration. As expected, the band gap increases from roughly 2.0 eV to 4.2 eV while electronic conductivity and magnetic susceptibility decrease the more Fe^{3+} is substituted by Al^{3+}. In addition, it was found that pure zinc ferrite, at least, exhibits conductivity dependent on the partial pressure of oxygen at temperatures above 600 °C. This could be an indication of possible oxygen-ion conductivity in the high-temperature range. Furthermore, special focus is put on the potential application of $ZnFe_{2-x}Al_xO_4$ with $x \leq 1.0$ as active material at the positive electrode of zinc-metal batteries. Zinc (de)insertion is investigated by cyclovoltammetric measurements in spinel|buffered aq. electrolyte|Zn cells. Results show that apart from zinc ions a considerable amount of protons can be reversibly co-inserted into the material, making it a possible contender as a stable active material.

1. Introduction

$ZnFe_2O_4$ (Franklinite) is a naturally occurring mineral, as is $ZnAl_2O_4$ (Gahnite). Both minerals belong to the spinel group (the mineral that lends its name to the group has the chemical formula $MgAl_2O_4$). The cubic spinel structure (space group $Fd\bar{3}m$) is based on a close-packed oxygen lattice in which cations occupy interstitial tetrahedral (A) and octahedral (B) sites. In a normal spinel, divalent cations preferentially occupy one-eighth of the tetrahedral sites, while trivalent cations fill half of the octahedral sites, yielding the general formula AB_2O_4. $ZnFe_2O_4$ and $ZnAl_2O_4$ are typically considered normal spinels [1–4], where Zn^{2+} ions reside on the tetrahedral A sites and Fe^{3+} or Al^{3+} ions occupy the octahedral B sites. However, partial cation inversion can occur, particularly in $ZnFe_2O_4$ [5,6], leading to redistribution of Zn^{2+} and Fe^{3+} between A and B sites [4]. This inversion modifies the local electronic structure [6], cation–anion bonding environment, and consequently the electrochemical behavior, as the availability of redox-active Fe species and diffusion pathways are directly influenced by the degree of site disorder.

The endmember $ZnFe_2O_4$ is a well-known material for photocatalytic applications [3,7], which also shows interesting magnetic properties [4]. Apart from this, it has also been successfully tested as active material at the negative electrode in lithium-ion batteries (LIB) [4] and at the positive electrode of zinc-ion or zinc-metal batteries (ZIB/ZMB) [8]. $ZnAl_2O_4$ has been investigated for photocatalytic applications as well [9], but also for its potential application in supercapacitors, optical applications [10], and for the oxygen evolution reaction [11]. In context of energy materials, it has been analyzed as possible coating for LIB cathode materials such as e.g. $LiFePO_4$ [12] or lithium spinels [13] to improve structural stability and electrochemical performance.

$ZnFe_{2-x}Al_xO_4$ with an aluminum content of $0 < x \leq 1$ should prove useful for improving chemical stability for use as active materials in

* Corresponding author.
E-mail address: k.neuhaus@fz-juelich.de (K. Neuhaus).

https://doi.org/10.1016/j.ssi.2026.117205
Received 9 February 2026; Received in revised form 1 April 2026; Accepted 2 April 2026
Available online 9 April 2026

zinc-metal batteries. It is already known from the literature that doping with aluminum has a positive effect on the chemical stability of zinc ferrite when applied in LIBs, while also decreasing the electrical conductivity [14]. The improvement in chemical stability [15] could potentially also reduce Fe^{2+} leaching from $ZnFe_{2-x}Al_xO_4$ and subsequent structural decomposition in contact with aqueous electrolytes in ZIB. Leaching so far is one of the major problems for Fe- as well as Mn-based oxidic active materials in contact with slightly acidic electrolytes [16]. However, by maintaining a comparably high iron content, the cell voltage should be elevated compared to pure $ZnAl_2O_4$ and also the comparably high electronic conductivity of $ZnFe_2O_4$, which is favorable for good charge transport within the active material, should be maintained to some extent. In addition to changes in the electronic conductivity, a continuous change of magnetic properties due to the variation of the iron content and associated $Fe^{2+/3+}$ redox is expected across the entire series.

For this reason, we present experimental work on the structural, physical and electrochemical properties of samples of the solid solution series $ZnFe_{2-x}Al_xO_4$ with $x = 0.0$ to 2.0. To date, there is no comprehensive experimental data on the electrical conductivity of partially Al-substituted zinc ferrites. Hence, the electrical conductivity as well as performance in ZMB cells was evaluated in combination with the magnetic susceptibility and optical reflectance. Operation in battery cells was analyzed only for materials with the composition $0 \leq x \leq 1$, to ensure a sufficiently high Fe concentration to maintain high electronic conductivity.

2. Experimental section

2.1. Material synthesis and sample preparation

Samples were produced via a Pechini-type synthesis process: To this end, $Zn(NO_3)_2 \bullet 6H_2O$, $Fe(NO_3)_3 \bullet 9H_2O$, and $Al(NO_3)_2 \bullet 9H_2O$ were mixed in distilled water according to the nominal composition. When the salts were fully dissolved, citric acid (ncitric acid = 2ncations) was added and the mixture was stirred for 1 h at 50 °C. Afterwards, 1,4-butylene diol was added (ndiol = 4ncations), the temperature was increased to 80 °C and stirred for further 30 min. Then, the temperature was increased to 300 °C to dry the gel. The gel was put in glazed alumina crucibles and calcined at 200 °C for 2 and then 600 °C for 4 h in a muffle furnace. The received powder was thoroughly ground in an agate mortar and either used to press pellets for analyses in materials level, or the calcined powder was used to prepare electrode sheets. On the one hand, this made it possible to obtain materials with a high defect content, which is beneficial for high capacity when used as active material [17]. On the other hand, the additional sintering step for the tablets made it possible to obtain dense, low-defect samples for impedance measurements and structural analysis. Pellets were pressed with a pressure of 100 bar and sintered at 1200 °C for 6 h in alumina sintering boxes with a heating/cooling rate of 200 K/h.

The calcined powders were used to prepare the slurry, using polyvinylidene fluoride (PVDF) as a binder (provided as a 10% solution in *N*-methyl-2-pyrrolidone (NMP)) and carbon black as conducting agent. These three components were mixed in an 80:10:10 weight ratio. Additionally, 2 mL of NMP was added to the mixture, which was then stirred overnight to ensure uniform dispersion. The resulting slurry was coated onto 25 μm-thick titanium foil in a 200 μm-thick layer. The coated sheets were then dried at 80 °C for approximately 6 h to remove excess solvent. Once dried, the sheets were punched into 12 mm electrodes. A final drying step was performed under vacuum at 110 °C for 12 h to eliminate any remaining solvent residues.

2.2. Structural characterization

Powder X-ray diffraction (PXRD) measurements were carried out to investigate the structural properties of the materials on a Panalytical Empyrean DY 2785 with Cu Kα radiation (λ = 1.54 Å, Bragg-Brentano geometry) and an acceleration voltage of 40 kV. The step size was set to 0.013° over a 2θ range of 5 to 130°. Further, PXRD measurements of selected compositions were performed on a Panalytical Empyrean DY 1473 with Mo Kα radiation (λ = 0.71 Å, Debye-Scherrer geometry) and an acceleration voltage of 55 kV. The step size was set to 0.008° over a 2θ range of 5 to 55°.

Additionally, $ZnFeAlO_4$ was investigated by neutron diffraction at the ILL (Institute Laue Langevin) on the D2B beamline. The measurement was taken with a wavelength of 1.594 Å over a 2θ range from 0 to 160° and a 200 mm slit.

The structural refinements were performed using Diffrac.Topas (Bruker) applying the fundamental parameters approach. In the refinements, measurements of different radiation were coupled, coupling refinable parameters onto each other. Before performing the Rietveld refinement, a Pawley refinement was carried out to determine the microstructural contribution to the fitted model.

2.3. Electrochemical characterization

2.3.1. Impedance spectroscopy measurements

To analyze the electrical conductivity of the materials at RT-80 °C, impedance spectroscopy measurements were performed on the ceramics, which were sputtered with Au electrodes on both sides to generate ideal contacts. Impedance spectroscopy measurements were performed using a potentiostat M204 (Metrohm GmbH & Co. KG, Germany). At temperatures above 100 °C, measurements were performed with an AutoLab IMP potentiostat (Metrohm GmbH & Co. KG, Germany) in an ROK 70/250/12 oven (ThermoConcept GmbH, Germany) in a frequency range of 1–10^6 Hz with an excitation voltage of 0.04 V.

2.3.2. Cyclovoltammetry measurements

For cyclovoltammetry (CV) measurements, Swagelok cells were investigated with a potentiostat M204 (Metrohm GmbH & Co. KG, Germany). The cells were built with electrodes from calcined spinel powders as the positive electrode and zinc foil as the negative electrode. The electrolyte was prepared from a commercial pH 5 buffer solution (Reagecon, Ireland: potassium hydrogen-phthalate and sodium hydroxide as buffer as well as potassium iodide, chloride, and minute amounts of mercury iodide as additive) with 3 M $Zn(OTf)_2$ as conductive salt. The measured potential window was between 0.8 and 1.7 V against a Zn/Zn^{2+} reference at a scan rate of $\nu = 0.2$ mV s^{-1}.

2.3.3. Hebb-Wagner measurements

Hebb-Wagner-type measurements with a Pt microcontact (as described in ref. [18]) were used to determine the electronic partial conductivity data of the samples in dependence on oxygen partial pressure and temperature. Measurements were performed with an AutoLab IMP potentiostat (Metrohm GmbH & Co. KG, Germany) in an ROK 70/250/12 oven (ThermoConcept GmbH, Germany). The ceramics pellets were contacted at the bottom with a platinum sheet and additionally fixed with platinum paste (fuelcellmaterials, USA) as counter electrode, and on top with a Pt microcontact as working electrode. The microcontact was encapsuled with a glass paste IP211 (Heraeus Deutschland GmbH & Co.KG, Germany) and annealed at 950 °C for 15 min. Measurements were taken from 850 °C to 400 °C with a two-hour holding period prior to each measurement.

2.4. Optical analysis

An Edinburgh Instruments FS920 spectrometer equipped with a 450 W Xe900 arc lamp and a R928 detector from Hamamatsu combined with a Teflon-coated integrating sphere was used to analyze the reflection of the samples to determine the optical band gap. Measurements were initially taken in the wavelength range from 250 nm to 500 nm with a step size of 1.0 nm and then from 480 nm to 800 nm with a 455 nm filter

and a step size of 1.0 nm. Both spectra were then combined at 490 nm. Barium sulfate ($BaSO_4$; 99.99%; Sigma-Aldrich) was used as reference.

2.5. Magnetic properties

A typical instrument to measure the magnetic susceptibility of a given material is the Evan's balance. The working principle is that two small permanent magnets are supported by a suspension strip. The force that the sample exerts on one of the magnets is balanced by a current through a coil placed between the poles of the other magnet. The current measured through the coil is proportional to the force exerted by the sample. In this study, a JM Auto Magnetic Susceptibility Balance was used, which directly indicates the material's volume susceptibility. Crushed powder from the sintered ceramics was used for these measurements.

3. Results and discussion

3.1. Structural analysis

Powder XRD measurements (PXRD spectra can be found in Supporting Information 1) show that the lattice parameter of the samples, as depicted in Fig. 1A, decreases linearly with increasing Al concentration. Accordingly, the theoretical density of the material also becomes increasingly lower (Fig. 1B). The relative measured density is in the range of 95% up to a composition of x = 1.0, after which the porosity of the material increases.

A common measure of the degree of inversion—apart from the peak ratio obtained from XRD—is the anion parameter (cf. Fig. 1C). At an aluminum content of x = 0.2, the anion parameter reaches its minimum, while the difference in bond lengths is at its maximum. Moreover, when comparing the determined anion parameters with the thresholds reported by Sickafus et al. [19], all samples lie above the limit for an inverse spinel. Starting from x = 0.2, the anion parameter increases again, indicating that the structure becomes progressively more normal with increasing aluminum content. Similar to the lattice parameter, metal-oxygen bond distances decrease with increasing aluminum content. In octahedral coordination, the bond distances change only slightly at low aluminum concentrations. From x = 0.6 to 2 stoichiometric units, the decrease is linear. Due to the difference in ionic radius between Fe^{3+} and Al^{3+}, the bond distances decrease from 2.0179(7) Å to 1.9146(3) Å.

Further investigations regarding the position of the different cations in the spinel structure showed that Zn is preferably located on the tetrahedral sites while aluminum and iron are mainly located on the octahedral lattice sites (cf. Table 1). This is particularly relevant in the context of the potentially high inversion ratio between Zn^{2+} and Fe^{3+} in $ZnFe_2O_4$ described in the introduction, since the variations in physical properties described below are thus primarily attributable to the substitution of Fe^{3+} with Al^{3+} and are not substantially influenced by a

Table 1
Predicted and adjusted chemical composition of each sample from XRD measurements. In the calculated composition, the cations are allocated between tetrahedral and octahedral sites.

Expected	Calculated
$ZnFe_2O_4$	$ZnFe_2O_4$
$ZnFe_{1.8}Al_{0.2}O_4$	$[Zn_{0.985}Al_{0.01}]^{tet}[Fe_{1.87}Al_{0.128}]^{oct}O_4$
$ZnFe_{1.6}Al_{0.4}O_4$	$[Zn_{0.972}Al_{0.028}]^{tet}[Fe_{1.614}Al_{0.396}]^{oct}O_4$
$ZnFe_{1.4}Al_{0.6}O_4$	$[Zn_{0.956}Al_{0.042}]^{tet}[Fe_{1.37}Al_{0.628}]^{oct}O_4$
$ZnFeAlO_4$	$[Zn_{0.965}Al_{0.025}Fe_{0.01}]^{tet}[Zn_{0.104}Fe_{0.904}Al_{0.992}]^{oct}O_4$
$ZnAl_2O_4$	$[Zn_{0.948}Al_{0.052}]^{tet}[Al_2]^{oct}O_4$

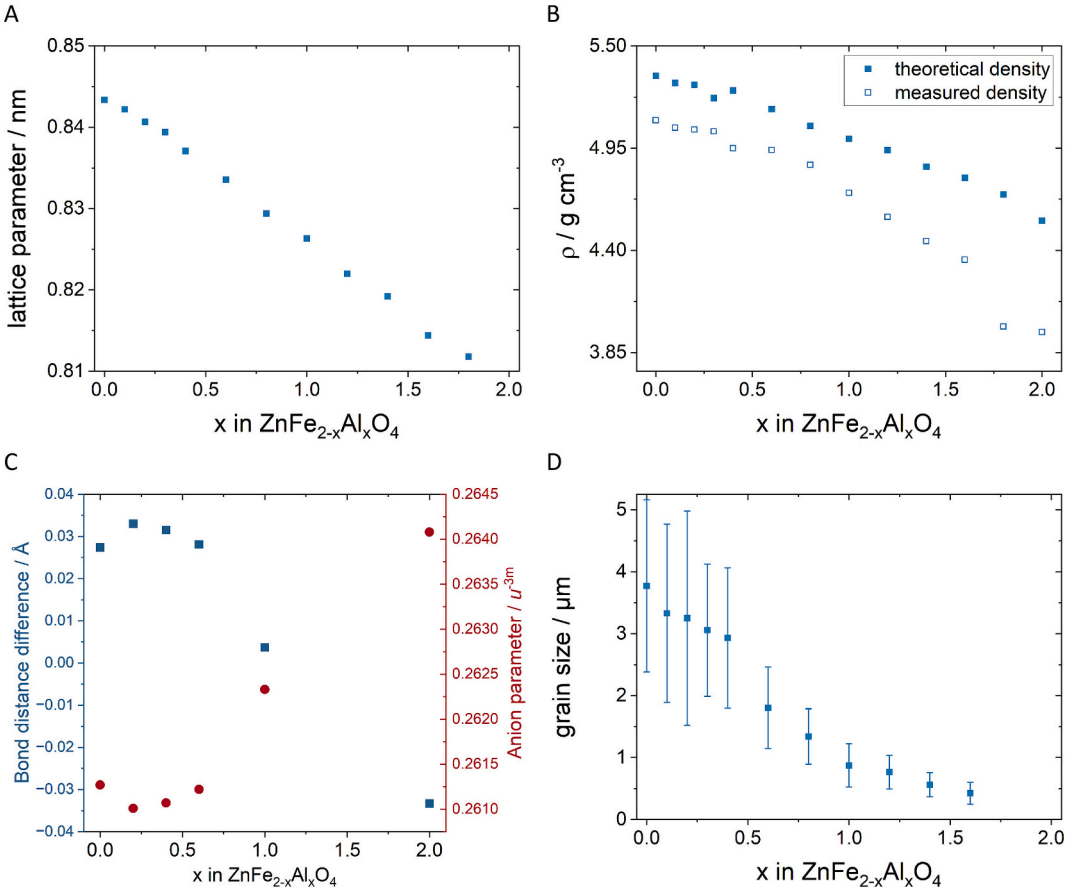

Fig. 1. (A) Lattice parameter, (B) theoretical and measured averaged density and (C) average grain size of the samples in dependence on aluminum concentration.

change in the inversion ratio.

The grain size after sintering also strongly depends on the aluminum content (see Fig. 1D and Supporting Information 2): all samples between x = 0.0 and x = 0.4 showed relatively large grains with a broad grainsize distribution. At high aluminum content the average grain sizes became distinctly smaller with grains below 1 μm at x ≥ 1.0. For x = 1.8 and x = 2.0, the grain size became very small and grain boundaries were less well defined so that the average grain size was not determinable. This suggests that the sintering temperature of 1200 °C, which was optimized for pure $ZnFe_2O_4$ [8], is optimal for an Al concentration of up to x = 1.0. After that, slightly higher sintering temperatures and/or longer holding times could probably produce denser samples with larger grains.

3.2. Charge transport and zinc-ion insertion

3.2.1. Electrical conductivity

Pure zinc ferrite is known to have a comparably high electrical conductivity which is governed by electron conductivity [4,8]. From the results shown in Fig. 2A and B it can be observed that around x = 0.2 to x = 0.3, the electrical conductivity is comparable to the pure zinc ferrite. This comparably high electronic conductivity is also accompanied by a minimum of the activation energy (Fig. 2C). The large standard deviation for the activation energy for pure $ZnAl_2O_4$ can be attributed to the fact that the electrical conductivity was very low. Therefore a certain error must be taken into account both when fitting the functions in the impedance evaluation and in the linear fit to determine the activation energy.

The electrical conductivity and activation energy for pure ferrite is lower than previously published data from our group indicate [8], but comparable to values measured by other groups for low inversion zinc ferrite [6]. The lower degree of inversion may have been caused by a slightly modified calcination step in the powder preparation process compared to previously published materials. For $ZnAl_2O_4$ nanoparticles, pronouncedly higher electrical conductivity in the range of 1 $S \bullet cm^{-1}$ between 20 and 80 °C has been reported [20]. However, this seems unrealistic in our case, since our samples have a wide band gap and the ionic conductivity is unlikely to be in this range.

The significant decrease in electrical conductivity that accompanies the increasing substitution of Fe^{3+} with Al^{3+} can be attributed primarily to a decrease in electronic conductivity. This dominates conduction in pure zinc ferrite [4] and is generated by small-scale polaron hopping via the Fe^{2+}/Fe^{3+} redox system [21]. As transport pathways via reducible Fe^{3+} ions are gradually eliminated—since Al^{3+} cannot be reduced—this type of charge transport also decreases. However, a slight Al doping in the region where the deviation from a linear relationship is observed here could lead to increased ionic conductivity within a small composition window.

Apart from analyses at low temperature, $ZnFe_2O_4$, $ZnFeAlO_4$ and $ZnAl_2O_4$ were also investigated for the conductive properties at temperatures between 400 and 850 °C. The redox process $Fe^{2+/3+}$ is in an accessible oxygen partial pressure range at temperatures above 500 °C and should strongly affect the electronic properties of the Fe-containing spinels. In addition, there recently have been reports on BaX_2O_4 (X = Nd, Sm) with spinel structure which showed electronic as well as oxygen ion and proton conductivity at elevated temperatures [22].

In order to obtain information on the onset of Fe-redox and to assess whether oxygen ion conductivity could potentially occur in the materials examined at elevated temperatures, the total conductivity and the oxygen partial pressure dependent electronic conductivity were measured by impedance spectroscopy and using a Hebb-Wagner setup, respectively (cf. Fig. 3). In the past, this setup has already been used to successfully investigate the oxygen partial pressure-dependent electronic partial conductivity of various oxygen ion conductors [18,23,24].

As expected, $ZnAl_2O_4$ and $ZnFeAlO_4$ exhibit significantly lower

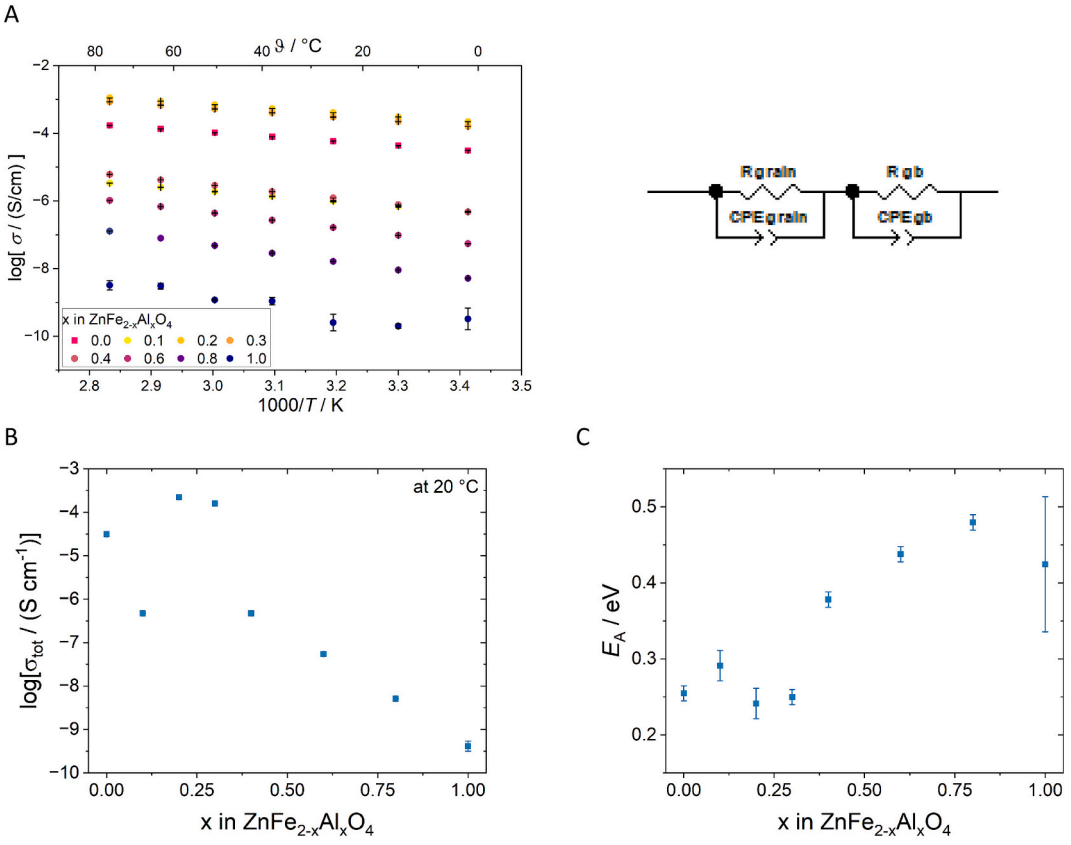

Fig. 2. (A) Electrical conductivity of all compositions with 0 ≤ x ≤ 1 in dependence on temperature between 20 and 80 °C with the equivalent circuit used for analysis and (B) at a fixed temperature of 20 °C as measured by impedance spectroscopy. (C) Activation energy calculated from electrical conductivity measurements.

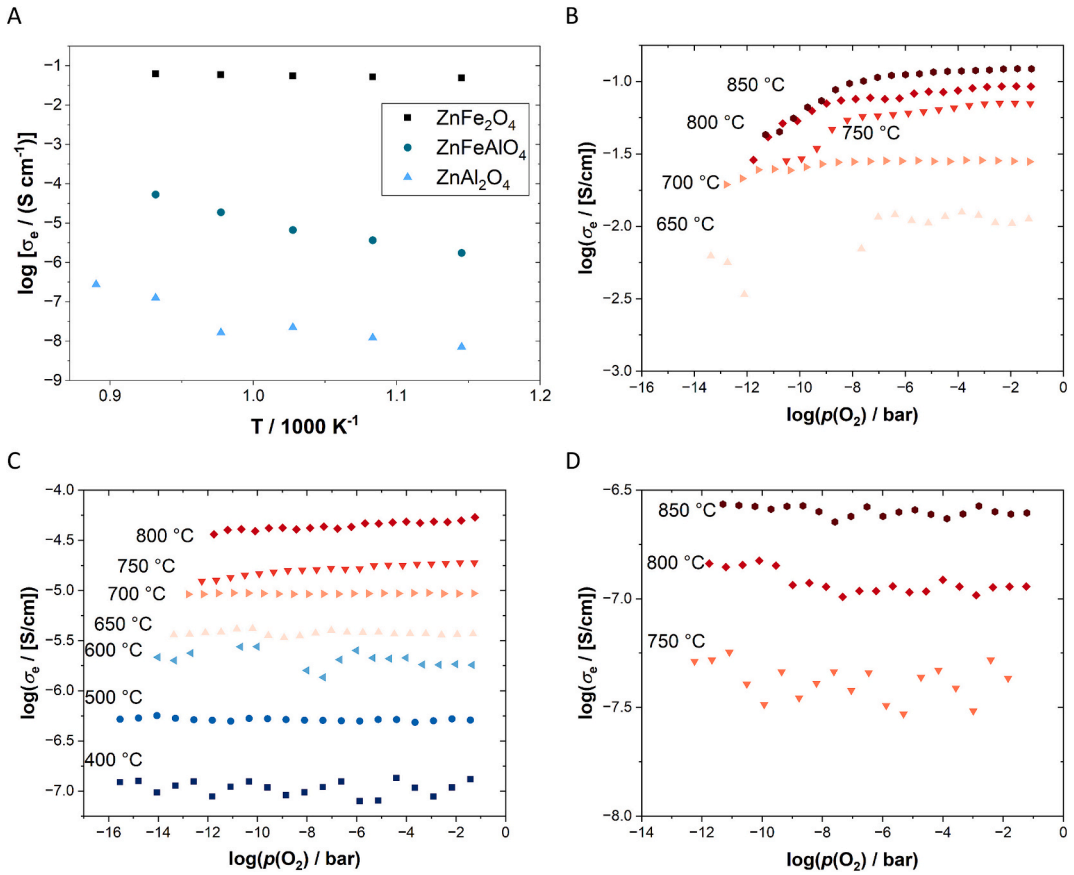

Fig. 3. A) Electron conductivity of all three samples at an oxygen partial pressure of 0.21 bar. This conductivity was comparable to the electrical conductivity measured by impedance spectroscopy. B) Oxygen partial pressure-dependent electron conductivity of $ZnFe_2O_4$. C) Oxygen partial pressure-dependent electron conductivity of $ZnFeAlO_4$. D) Oxygen partial pressure-dependent electron conductivity of $ZnAl_2O_4$.

electron conductivity even at high temperatures (see Fig. 3A). In addition, the activation energy for electron transport is much lower for $ZnFe_2O_4$ with 0.10 ± 0.01 eV than for $ZnFeAlO_4$ with 1.36 ± 0.14 eV, and $ZnAl_2O_4$ with 1.19 ± 0.27 eV, respectively. Both Al-containing samples also show an almost flat profile of the electron conductivity with no obvious dependence on the oxygen partial pressure. In addition, the measurements with $ZnAl_2O_4$ show very strong noise, as the electron conductivity here is already close to the detection limit of the device. Temperatures below 750 °C were not analyzable due to this. For $ZnFe_2O_4$, measurements below 650 °C became also very noisy because the $Fe^{2+/3+}$ redox reaction slows down and leads to pronounced variation of the necessary polarization times with varying applied voltage. However, for $ZnFe_2O_4$, there can be found a clear drop in electronic conductivity at temperatures above 700 °C and oxygen partial pressures below 10^{-8} bar which is at a somewhat lower oxygen partial pressure than the $Fe^{2+/3+}$ transition, which was observed when having Fe as a sintering additive in oxygen ion conductive ceria compounds [25].

Impedance spectroscopy measurements at the same temperatures at ambient oxygen partial pressure showed that the electrical conductivity of all three compounds is governed by the electronic conductivity, so the difference between measured electron conductivity and electrical conductivity was in the range of error due to different measurement setups.

3.2.2. *Reflection spectroscopy*

As can already be assumed from the color change of the samples with $ZnFe_2O_4$ being dark brown and $ZnAl_2O_4$ cream white, the optical band gap of $ZnFe_{2-x}Al_xO_4$ increases considerably with increasing Al concentration (see Fig. 4). For x = 0.0 to x = 0.3, E_g is in the range of the values reported for pure $ZnFe_2O_4$ of around 2.02 eV [4,8] (but much lower than reported for Al-doped $ZnFe_2O_4$ nanoparticles in ref. [26]). This fits very

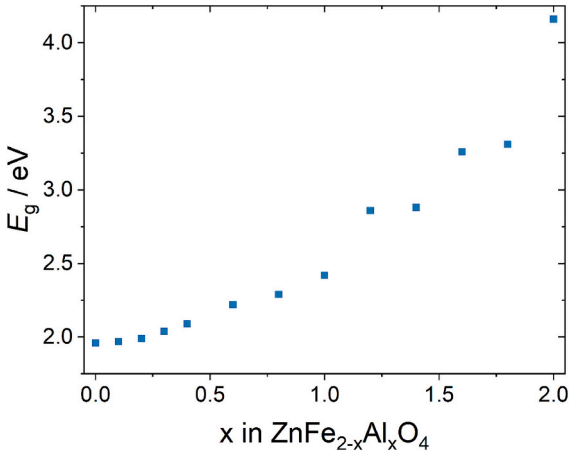

Fig. 4. Optical band gap of $ZnFe_{2-x}Al_xO_4$ as function of x. All values roughly have an error of ±0.1.

well with the observed local maximum of electrical conductivity and minimum of activation energy from impedance measurements. At concentrations above x = 0.5 the band gap energy begins to rise sharply, reaching a value of 4.16 ± 0.1 eV for pure $ZnAl_2O_4$, which is roughly 1.25 eV less than values found for $ZnAl_2O_4$ nanoparticles in literature (about 5.45 eV) [1,2,10]. Similar to the discrepancies between micrometer-scale $ZnFe_2O_4$ and nanoparticles with the same composition, this can be attributed to grain boundary effects, which occur in ground ceramic materials but not in nanoparticles.

3.2.3. Cyclovoltammetry

In the cyclic voltammetry measurements with aqueous electrolyte, all samples except for x = 1.0 show a relatively broad oxidation peak at about 0.92 V (denoted as O3 in Fig. 5). In addition, all measured samples show a distinct, sharper peak in the range between 1.2 and 1.3 V (O2) and, in some samples, an additional oxidation peak at about 1.42 V vs. Zn/Zn^{+2} (O1). For the reduction, two broader peaks (R2 at about 1.08 V and R1 at about 1.22 V vs. Zn/Zn^{+2}) can be observed in all measurements (see Fig. 5). This means, we have a potential difference of 0.2 V for O1/R1 and of roughly 0.17 V for O2/R2.

The oxidation peak O2 which moves between 1.2 and 1.3 V vs. Zn/Zn^{+2} and the corresponding reduction peak R2 can be assigned to proton insertion/deinsertion into the spinel material. To show this, CV measurements of a cell without Zn conductive salt are shown in Fig. 6A. Despite the absence of Zn^{2+} in the electrolyte, clear oxidation and reduction peaks at the position of O2/R2 can be observed. Proton co-insertion is a common phenomenon which has also been observed for different manganese oxide active materials in context with aqueous electrolytes [27]. However, to rule out proton co-insertion in the carbon component of the cathode as a parallel process, cells with pure Super P cathodes without spinel active materials were built and tested with buffer solution with and without zinc conductive salts. These

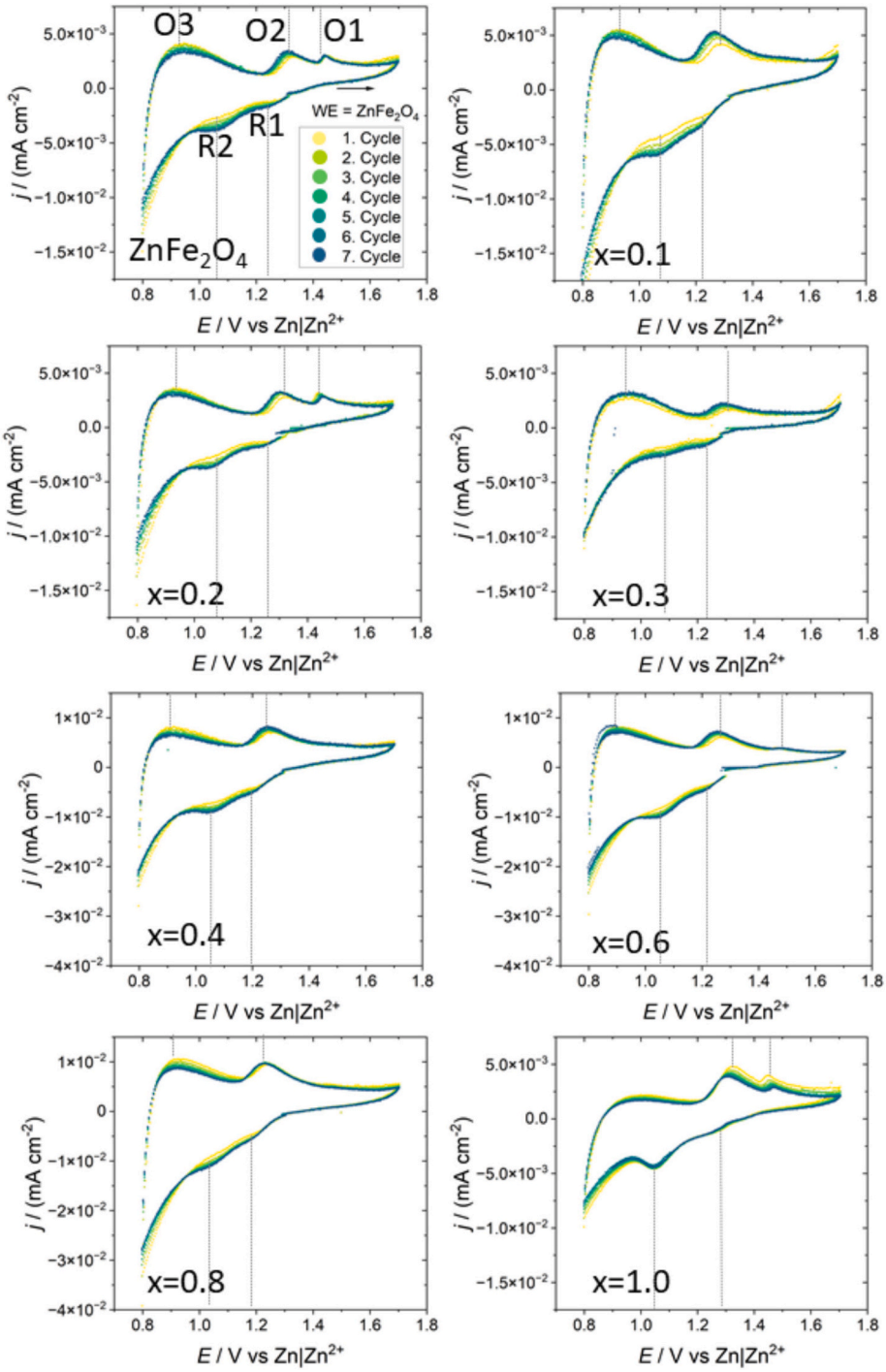

Fig. 5. Cyclic voltammograms recorded in a cell with $ZnFe_{2-x}Al_xO_4||Zn(OTf)_2$ in pH 5 buffer solution|Zn foil at a scan rate of $\nu = 0.2$ mV s^{-1}. The grey dotted lines indicate the positions of oxidation and reduction peaks in the first cycle.

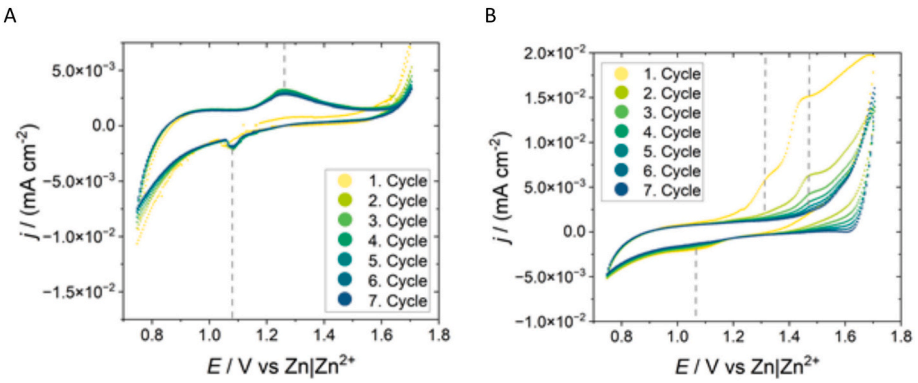

Fig. 6. (A) Cyclovoltammetry measurements of a cell with $ZnFeAlO_4$|pH 5 buffer solution|Zn foil at a scan rate of $\nu = 0.2$ mV s^{-1}, no zinc salt added. Clear oxidation and reduction peaks are visible despite the absence of conductive salt. These peaks can be assigned to proton (de)insertion in the spinel material. (B) Cyclovoltammetry measurements of a cell with $ZnFeAlO_4$|0.5 M $Zn(OTf)_2$ in acetonitrile|sputtered Zn on Ti foil at a scan rate of $\nu = 0.2$ mV s^{-1}.

measurements showed no insertion behavior (no measurable current density) in the first 5–8 cycles. Afterwards, the current density is slightly increased but without a strong hysteresis between the directions. This could be due to small-scale side reactions with the electrolyte, showing that the combination of $Zn(OTf)_2$ and the buffer solution of potassium hydrogen phthalate and sodium hydroxide is not the optimal choice for long-term operation.

In principle, proton co-insertion could be used as an additional means to transport charge within a ZMB, but it poses problems related to strong local changes of the electrolyte pH during cycling. These can possibly be mitigated by using suitable buffers, but still pose a challenge in terms of parasitic reactions.

The small peaks O1 and R1 in Fig. 5, which are not well visible for some of the compositions, can be assigned to Zn^{2+} (de)insertion in the material. To demonstrate this, CV measurements of $ZnFeAlO_4$ in organic electrolyte (0.5 M $Zn(Otf)_2$ in acetonitrile) were performed in addition to the measurements in aqueous electrolyte (Fig. 6B). Here, protons are not available and the only insertable species is Zn^{2+}. However, in the first cycle, an additional oxidation peak at about 1.3 V is visible, which could be due to the presence of a small amount of protons (e.g. residual moisture from the cathode, which was stored in air). This peak is not visible anymore in the following cycles. In addition, there is a small reduction peak 1.06 V, which could also be due to proton insertion.

The potential for the peak associated with zinc de-insertion is slightly lower than was found for $ZnFe_{1.91}Ti_{0.09}O_4$ [8], where a potential between 1.55 and 1.65 V vs. Zn/Zn^{2+} for the oxidation peak during anodic sweep was observed using an organic electrolyte. A peak associated to zinc insertion into the spinel could not be observed, which is in accordance with the observations for $ZnFe_{1.91}Ti_{0.09}O_4$ [8].

Overall, we conclude that materials with compositions up to $ZnFeAlO_4$ are potentially suitable as active materials for the cathode side in zinc metal batteries. The redox-reactions in the CV curves are reversible for all compositions and do not show a significant change in current density over ten cycles. Further measurements over 20 cycles also yielded consistent results. This can serve as an initial indication of good cycle stability of the material in combination with the buffered aqueous electrolyte composition used here. At the same time, it must be taken into account that, in addition to zinc ions, protons are apparently also reversibly stored in the material. This is typical behavior for active materials in zinc-metal batteries (such an MnO_2 or $ZnMn_2O_4$ [16,28,29]); however, it can lead to significant fluctuations in the local pH distribution within the cell during charging and discharging, and consequently to pronounced side reactions. This once again underscores the importance of using a buffered electrolyte system.

3.3. Magnetic properties

Ferrite spinels are expected to be paramagnetic (pure $ZnFe_2O_4$ ceramics can be picked up with a conventional magnet [8]) because the magnetic behavior is governed by the Fe^{3+} ions, which have unpaired 3d electrons and therefore carry magnetic moments. In a normal spinel structure, Zn^{2+} occupies the tetrahedral sites while Fe^{3+} ions sit on the octahedral sites, where their magnetic moments are only weakly coupled, leading to paramagnetic behavior at room temperature. When an increasing number of Fe^{3+} ions are substituted by Al^{3+}, the overall number of magnetic ions decreases, since Al^{3+} has no unpaired electrons and is therefore non-magnetic. This substitution weakens any possible magnetic interactions even further, but does not introduce long-range magnetic ordering. As a result, the material remains paramagnetic, typically with a reduced magnetic susceptibility compared to the pure compound. As expected, all measured components except for pure $ZnAl_2O_4$ are paramagnetic ($\chi > 0$), with the magnetic susceptibility decreasing with increasing Al^{3+} concentration (see Fig. 7).

The values for pure $ZnFe_2O_4$ are somewhat lower than those previously reported for nanocrystalline $ZnFe_2O_4$ particles ($\chi = 6.6 \times 10^{-4}$ emu·g^{-1}·Oe^{-1} [30] which can be calculated to $\chi_V = 3.4 \pm 0.3 \bullet 10^{-3}$, when using the measured density for $ZnFe_2O_4$ from Fig. 1B). However, just as with optical measurements, the difference in particle size between nanoparticles and ground ceramic materials can play a role here. In addition, the degree of inversion also has a significant influence on magnetic susceptibility.

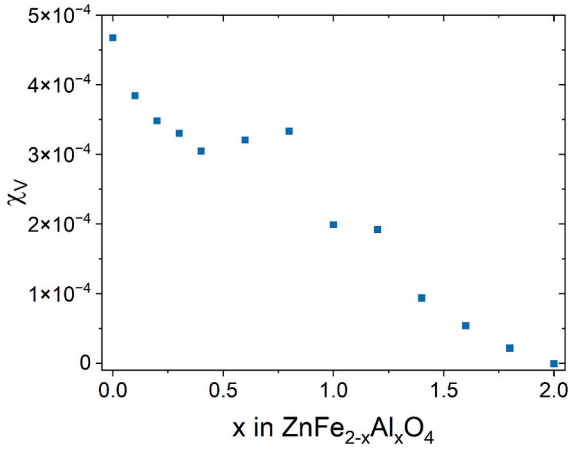

Fig. 7. Volumetric magnetic susceptibility of $ZnFe_{2-x}Al_xO_4$ as function of x.

4. Conclusions and Outlook

In summary, it has been shown that the physicochemical properties of the spinels investigated in this work depend heavily on the aluminum concentration and vary more or less linearly with it. A linear change of most characteristics from Franklinite to Gahnite is to be expected, particularly in terms of electronic conductivity, but also in terms of magnetic properties. However, at low aluminum concentrations, there is a sweet spot in the range around x = 0.25, where the electrical conductivity is particularly high and the activation energy particularly low, while at the same time the optical band gap is still very similar to that of pure $ZnFe_2O_4$. This range is especially interesting for use as an active material in ZMB, but also in other battery types, as on the one hand, the highest ionic conductivity of the system can be expected here, while at the same time a certain stabilization of the structure during zinc deinsertion is already achieved by the non-redox-active Al^{3+} on roughly 1/8 of the octahedral sites.

Interestingly, reversible zinc (de-)insertion can still be demonstrated via CV measurements even at much higher aluminum concentrations. However, proton (de-)insertion, similar to Mn-based oxides, for example, accounts for a not negligible proportion of the total capacity of the cell, which in most cases even significantly exceeds the current density of the peaks caused by zinc (de)insertion in the CV measurements shown. This means that when using the material together with aqueous electrolytes, measures must be taken to stabilize the pH value in the electrolyte (e.g. by using buffers as done here) in order to minimize local parasitic reactions such as hydrogen formation or the formation of basic zinc salts.

Regardless of its use as an active material, a dependence of electronic conductivity on oxygen partial pressure was also determined for $ZnFe_2O_4$ at high temperatures above 700 °C. This suggests that at least $ZnFe_2O_4$ could also transport oxygen ions in this temperature range. To date, there have been very few reports of oxygen ion conductors with a spinel structure, so further investigations into the permeation properties would certainly be interesting here due to the comparatively high electron conductivity.

In addition to their importance for applications as energy materials, this study is also relevant for geological systems, since franklinite, gahnite, and the corresponding mixtures can occur as associated minerals in zinc ore mines.

CRediT authorship contribution statement

Meriem Machitouen: Investigation, Formal analysis, Data curation. **Patrick Mowe:** Writing – review & editing, Formal analysis, Data curation, Conceptualization. **Johannes Spiegel:** Investigation, Formal analysis, Data curation. **Susanna Krämer:** Methodology, Investigation, Formal analysis, Conceptualization. **Rüdiger-A. Eichel:** Resources. **Martin Winter:** Validation, Resources. **Thomas Jüstel:** Validation, Supervision, Methodology. **Anna Windmüller:** Validation, Supervision, Formal analysis, Data curation, Conceptualization. **Kerstin Neuhaus:** Writing – original draft, Visualization, Validation, Supervision, Methodology, Investigation, Funding acquisition, Formal analysis, Data curation, Conceptualization.

Author statement

Meriem Mechitouen: Investigation, Writing Original Draft, Visualization.

Patrick Mowe: Investigation, Writing Review and Editing, Visualization, Validation.

Johannes N. Spiegel: Investigation, Writing Original Draft, Visualization, Writing Review and Editing.

Susanna Krämer: Writing Review and Editing.

Rüdiger-A. Eichel: Supervision, Resources.

Martin Winter: Supervision, Resources.

Thomas Jüstel: Supervision, Methodology.

Anna Windmüller: Conceptualization, Supervision.

Kerstin Neuhaus: Conceptualization, Data Curation, Writing Original Draft, Writing Review and Editing, Funding Acquisition, Project Administration, Supervision.

Funding

P. Mowe is funded by the Deutsche Forschungsgemeinschaft, project number 523164409. The work presented here was carried out in preparation for the project 573589769, funded by the Deutsche Forschungsgemeinschaft.

Declaration of competing interest

There are no competing interests.

Acknowledgements

P. Mowe is funded by the Deutsche Forschungsgemeinschaft, project number 523164409. The authors thank Dr. Emmanuelle Suard from ILL for support for the neutron diffraction measurements of $ZnFeAlO_4$. The work presented here was carried out in preparation for the project 573,589,769, funded by the Deutsche Forschungsgemeinschaft.

Appendix A. Supplementary data

Supplementary data to this article can be found online at https://doi.org/10.1016/j.ssi.2026.117205.

Data availability

Raw data is available from Zenodo repository (see cited DOI).

References

[1] S. Ramachandran, et al., Rapid synthesis and characterization of pure and cobalt doped zinc aluminate nanoparticles via microwave assisted combustion method, J. Nanosci. Nanotechnol. 20 (4) (2020) 2382–2388.
[2] A. Roniboss, et al., Investigation of structural, optical and magnetic behavior of MAl2O4 (m = Zn and Co) nanoparticles via microwave combustion technique, Mater. Sci. Semicond. Process. 123 (2021) 105507.
[3] M. Sundararajan, et al., A comparative study on $NiFe_2O_4$ and $ZnFe_2O_4$ spinel nanoparticles: structural, surface chemistry, optical, morphology and magnetic studies, Phys. B Condens. Matter 644 (2022) 414232.
[4] M. Bohra, V. Alman, R. Arras, Nanostructured ZnFe2O4: an exotic energy material, Nanomater 11 (5) (2021) 1286.
[5] Q. Yuan, et al., Cation distribution and magnetism in quenched $ZnFe_2O_4$, J. Electron. Mater. 47 (7) (2018) 3608–3614.
[6] L.I. Granone, et al., Effect of the degree of inversion on the electrical conductivity of spinel ZnFe2O4, ChemistrySelect 4 (4) (2019) 1232–1239.
[7] M. Sundararajan, et al., Photocatalytic degradation of rhodamine b under visible light using nanostructured zinc doped cobalt ferrite: kinetics and mechanism, Ceram. Int. 43 (1) (2017) 540–548.
[8] S. Krämer, et al., Ti-doped ZnFe2O4 as active material in zinc ion batteries – a proof of concept, Energy Adv. 3 (2024) 2175–2185.
[9] S. Battiston, et al., Synthesis of zinc aluminate ($ZnAl_2O_4$) spinel and its application as photocatalyst, Mater. Res. 17 (2014) 734–738.
[10] T.S. Nirmala, et al., Third order nonlinear optical behavior and optical limiting properties of ni2+ ions doped zinc nano-aluminates, Opt. Mater. 124 (2022) 111950.
[11] S. Gouadria, et al., Development of bifunctional Mo doped ZnAl2O4 spinel nanorods array directly grown on carbon fiber for supercapacitor and OER application, Ceram. Int. 49 (3) (2023) 4281–4289.
[12] M. Moustafa, M.M. Sanad, Green fabrication of ZnAl2O4-coated LiFePO4 nanoparticles for enhanced electrochemical performance in li-ion batteries, J. Alloys Compd. 903 (2022) 163910.
[13] Y. Lee, et al., Surface modification of $LiNi_{0.5}Mn_{1.5}O_4$ cathodes with $ZnAl_2O_4$ by a sol–gel method for lithium ion batteries, Electrochim. Acta 115 (2014) 326–331.
[14] M. Ruiz, S. Jacobo, Electromagnetic properties of lithium zinc ferrites doped with aluminum, Phys. B Condens. Matter 407 (16) (2012) 3274–3277.
[15] Y. Tang, et al., Zinc stabilization efficiency of aluminate spinel structure and its leaching behavior, Environ. Sci. Technol. 45 (24) (2011) 10544–10550.
[16] Y. Aniskevich, S.-T. Myung, Gains and losses in zinc-ion batteries by proton-and water-assisted reactions, Chem. Soc. Rev. 54 (2025) 4531–4566.

[17] T.-H. Wu, W.-Y. Liang, Reduced intercalation energy barrier by rich structural water in spinel $ZnMn_2O_4$ for high-rate zinc-ion batteries, ACS Appl. Mater. Interfaces 13 (20) (2021) 23822–23832.
[18] K. Schmale, et al., Electronic conductivity of $Ce_{0.8}Gd_{0.2-x}Pr_xO_{2-\delta}$ and influence of added CoO, Phys. Status Solidi B 248 (2) (2011) 314–322.
[19] K.E. Sickafus, J.M. Wills, N.W. Grimes, Structure of spinel, J. Am. Ceram. Soc. 82 (12) (1999) 3279–3292.
[20] B. Goswami, G. Rani, R. Ahlawat, Insight into the crystalline structure, morphology, luminescence, and electrical conductivity of ZnAl2O4: XMn2+ (0≤ x≤ 2.0 Mol%) nanostructures, Phys. Scr. 98 (11) (2023) 115974.
[21] N. John, et al., Enhancing thermoelectric properties of spinel ZnFe2O4 by Ni substitution through electron hopping mechanism, Ceram. Int. 50 (22) (2024) 45251–45262.
[22] N. Tarasova, et al., Electrical conductivity of BaM2O4 (m = Nd, Sm) with a spinel structure, Chim. Techno. Acta 12 (4) (2025) 9038.
[23] J.-P. Eufinger, et al., The model case of an oxygen storage catalyst–non-stoichiometry, point defects and electrical conductivity of single crystalline CeO_2–ZrO_2 –Y_2O_3 solid solutions, Phys. Chem. Chem. Phys. 16 (46) (2014) 25583–25600.
[24] K. Schmale, et al., Influence of zinc oxide on the conductivity of ceria, J. Electrochem. Soc. 160 (9) (2013) F1081–F1087.
[25] A. Buchheit, et al., The impact of Fe addition on the electronic conductivity of gadolinium doped ceria, ECS J. Solid State Sci. Technol. 8 (1) (2019) P41.
[26] S. Gul, et al., Al-substituted zinc spinel ferrite nanoparticles: preparation and evaluation of structural, electrical, magnetic and photocatalytic properties, Ceram. Int. 46 (9) (2020) 14195–14205.
[27] L.E. Blanc, D. Kundu, L.F. Nazar, Scientific challenges for the implementation of Zn-ion batteries, Joule 4 (4) (2020) 771–799.
[28] N. Brandt, et al., Locally resolved operando pH measurement technique in aqueous zinc-manganese dioxide batteries, Electrochim. Acta 558 (2026) 148397.
[29] J. Pross-Brakhage, et al., Simulation-supported analysis of pH impacts on the voltage efficiency of aqueous zinc manganese dioxide batteries, J. Energy Storage 153 (2026) 120881.
[30] C. Yao, et al., ZnFe2O4 nanocrystals: synthesis and magnetic properties, J. Phys. Chem. C 111 (33) (2007) 12274–12278.